G D Conway

Effects of Reflectometer Asymmetries on Fluctuation Measurements

Effects of Reflectometer Asymmetries on Fluctuation Measurements

G D Conway.

JET Joint Undertaking, Abingdon, Oxfordshire, OX14 3EA,

ABSTRACT

Effects on reflectometer phase $\tilde{\phi}$ and power $\tilde{P}$ fluctuation signals due to (a) asymmetries in the transmit - plasma - receive antenna geometry (misalignments), and (b) asymmetries in the plasma cutoff layer perturbations (distortions from sinusoidal or Gaussian) are studied using a two dimensional (2D) physical optics model. Results show the onset of phase runaway with antenna misalignment and/or sawtooth type perturbations when the perturbation amplitude exceeds some critical value. For broadband (Gaussian) turbulence antenna misalignment leads to Doppler shifts in the $\tilde{\phi}$ spectrum - provided the reflectometer beam width w, and spectral width k_w of the turbulence are sufficiently large. Misalignment also generates coherence between $\tilde{\phi}$ and $\tilde{P}$ at Bragg backscatter frequencies with quadrature ($\pm\pi/2$) phase difference. Sawtooth (asymmetric gradient) perturbations also generate phase-power coherence in quadrature, but at frequencies determined by w and k_w, i.e. not Bragg. Cusped or spiky (asymmetric amplitude) perturbations generate asymmetric phase distributions (non-linear phase offsets) and low frequency phase-power coherence with 0 or π phase difference. The simulations indicate that a combination of antenna misalignment (or plasma tilt) and cusped reflection layer perturbations can account for a wide range of experimentally reported features in reflectometer signals.

1. INTRODUCTION

The use and sophistication of microwave reflectometry for measuring plasma fluctuations and turbulence in magnetically confined fusion experiments has grown steadily in recent years (for example see papers in [1-3]). Advances in hardware design have been accompanied by substantial progress in the understanding and interpretation of the reflectometer signals. Much of this progress has been achieved with the development of two dimensional (2D) modelling and simulation studies - which include full wave equations [4-6], WKB solutions [7,8], physical optics simulations [9-11] and others [12,13]. The various 2D models, despite their different approaches, appear to be converging on a consistent picture for the behaviour of reflectometer fluctuation signals; that is a realistic model is emerging for the instrument response function. Initial 2D simulation studies naturally concentrated on idealized reflectometer configurations, i.e. symmetric antenna patterns and symmetric angles for the launch and receive microwave beams, However, as confidence grows in the 2D models attention has begun to turn to the question of the effects of asymmetries in the geometry of the reflectometer configuration.

It has been widely suggested that asymmetry or misalignment between the launch and receive antennas and the plasma reflection layer may be responsible for the ubiquitous phase runaway effect observed in many experiments [14-20]. Indeed, recent simulations using 2D WKB codes [7,8] and distributed RLC networks [13] with asymmetric antenna angles are now revealing phase runaway effects.

Another form of asymmetry is distorted or non-symmetric plasma perturbations. For example, rotating magnetic islands have been proposed as a possible mechanism for generating sawtooth-like perturbations in the reflection layer [17], which again may lead to the reflectometer phase runaway effect. This paper presents, for the first time, a systematic study of the effects of asymmetries in the reflectometer geometry (misalignment), and asymmetries (distortions) in the reflection layer perturbations using a 2D physical optics model. The study includes the reflectometer's response to both single frequency plasma modes and broadband turbulence for non-normal incidence and backscatter, and with two forms of distorted layer perturbations - asymmetric amplitude (cusped) and asymmetric gradient (sawtooth) perturbations.

The simulations reveal many new features over previous studies, such as correlations between the phase and power signal fluctuations, as well as recovering the phase runaway and Doppler frequency shifts - which are shown only to appear in the presence of asymmetries. Many of the results reported here have been observed in experimental signals - indeed there is now a substantial body of evidence in the literature (for example [14,21,22,19,15-18,23]). However, it is beyond the scope of this paper to include an experimental example for each simulation result (space limitations notwithstanding) but where possible reference will be made to examples in the literature. Note that some early simulation results have already been compared with data from the JET reflectometers [24,25].

2. SIMULATION MODEL

The principle of plasma reflectometry is that a microwave beam of frequency ω_o propagates into a plasma until it reaches a cutoff condition and is reflected. For an O-mode polarized beam the cutoff condition is: $\omega^2_o = \omega^2_p$ (plasma frequency) while for an X-mode beam it is: $\omega^2_o = \omega^2_p \pm \omega_o \omega_c$ (plasma and cyclotron frequencies). Perturbations in the cutoff layer modulate the phase and amplitude of the reflected beam which are then measured using homodyne or heterodyne detection techniques.

To simulate the experiment the physical optics model uses the high spatial localization in the reflection of microwaves [21,26] to model the reflection layer as a thin distorted conducting surface. The phase and amplitude of the reflected microwave beam can then be calculated using the Helmholtz integral. The 2D physical optics model has previously been described in detail [27,10,11] but to incorporate non-normal incidence and reflection the 3D version is introduced. Using the same procedure (a far field Green's function) and notation as before [27,28] an expression for the scattered electric field is obtained:

$$E_2 = \frac{ik_o e^{ik_o d}}{4\pi d} \int_{-X}^{X} \int_{-Y}^{Y} e^{-\left(x^2/w_x^2\right)} e^{-\left(y^2/w_y^2\right)} \left(a\frac{\partial \zeta}{\partial x} + c\frac{\partial \zeta}{\partial y} - b \right) e^{i\left(v_x x + v_y y + v_z \zeta\right)} dxdy \qquad (1)$$

2

where

$$a = (1 - R)\sin\theta_1 - (1 + R)\sin\theta_2\cos\theta_3$$

$$b = (1 + R)\cos\theta_2 - (1 - R)\cos\theta_1$$

$$c = (1 + R)\sin\theta_2\sin\theta_3$$

$$v_x = k_o(\sin\theta_1 - \sin\theta_2\cos\theta_3)$$

$$v_y = k_o\sin\theta_2\sin\theta_3$$

$$v_z = -k_o(\cos\theta_1 + \cos\theta_2)$$

θ_1 is the angle of incidence relative to the (mean surface) normal, θ_2 is the scattering angle relative to the normal and θ_3 is the angle between the incident and scattering planes. Figure 1 shows a schematic of the geometry. The incident beam is a paraxial Gaussian beam (parallel wavefronts at the reflection layer) with an

Figure 1 : Schematic of model geometry. θ_1 and θ_2 are incident and scattered beam angles relative to the surface normal n in the plane parallel to the perturbation propagation vector. w_x and w_y are Gaussian beam radii at the layer. h and Λ are perturbation amplitude and wavelength.

elliptic cross section. w_x and w_y are the beam radii (elliptic half axis) in the x and y directions. $k_o = 2\pi/\lambda$ is the wavenumber of the incident microwave beam, R is the smooth surface reflection coefficient (in this case unity), and ζ is the perturbation displacement in the reflection layer (with respect to the mean).
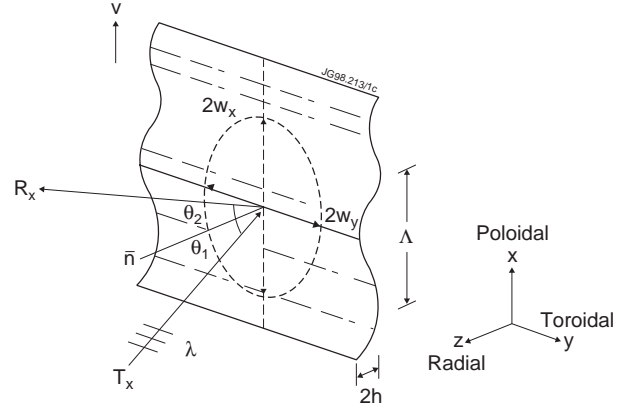
The far field solution of the Helmholtz integral (i.e. placing the transmit and receive antennas beyond the far field limit of both the fluctuations and the beam spot size) produces a general, non-configuration dependent solution by removing the antenna specific parameters such as size, location, and gain patterns etc. To remove the range d dependence the scattered field E_2 is normalized to the specularly reflected field from a smooth surface E_{20} to give the scattering coefficient $\rho = E_2/E_{20}$:

$$\rho = \frac{\int\limits_{-X}^{X}\int\limits_{-Y}^{Y} e^{-\left(x^2/w_x^2\right)}e^{-\left(y^2/w_y^2\right)}\left(a\dfrac{\partial\zeta}{\partial x} + c\dfrac{\partial\zeta}{\partial y} - b\right)e^{i(v_x x + v_y y + v_z \zeta)}\,dxdy}{2\cos\theta_1\int\limits_{-X}^{X}\int\limits_{-Y}^{Y} e^{-\left(x^2/w_x^2 - y^2/w_y^2\right)}\,dxdy} \tag{2}$$

Equation 2 can be solved numerically for any three dimensional surface perturbation $\zeta(x,y,z,t)$. However for the purpose of this work the expression for the scattering coefficient can be reduced to

$$\rho = \frac{\int\limits_{-X}^{X} exp(-(1 + \cos^2\theta_1)x^2/w^2)\left(a\dfrac{\partial\zeta}{\partial x} - b\right)exp\,i(v_x x + v_z\zeta)\,dx}{2\cos\theta_1\int\limits_{-X}^{X} exp(-(1 + \cos^2\theta_1)x^2/w^2)\,dx} \tag{3}$$

by making the following simplifications.

(1) Depolarization is ignored, only scattering in the plane of incidence is considered, i.e. $\theta_3 = 0$ (the scalar wave case). Although depolarization or cross-polarization scattering almost certainly occurs in the experimental situation, it's effect should be small.

(2) The incident microwave beam has a circular cross section, i.e. $w_x = w_y = w$. However for non-normal incidence the incident beam still produces an elliptic spot size or footprint on the surface. The $(1 + \cos^2 \theta_1)$ factor in the profile exponent accounts for this effect.

(3) The y direction is aligned along the magnetic field lines (toroidal) and x in the transverse (poloidal) direction. The toroidal correlation length of plasma density fluctuations is usually much larger than the spot size, i.e. $L_t \gg w$ while the poloidal length $L_p \leq w$. This assumption removes the y dependence in the perturbation displacement ζ and allows the 3D expression for ρ to be collapsed to an enhanced 2D expression. However this assumption may not be applicable in certain conditions. For example in the tokamak scrape-off layer (SOL) and divertor regions, rather than appearing as striations the density fluctuations may have a more granular structure, that is $L_t \approx w$. However, the full 3D solution will not be pursued in the current study.

The plasma perturbations are assumed to move under the reflectometer beam transverse to the magnetic field lines (in the poloidal direction) with a uniform constant velocity (linear dispersion relation). Simulated reflectometer power (amplitude squared) and phase time signals are then generated from

$$P(t) = \rho(t)\, \rho^*(t), \tag{4}$$

$$\phi(t) = \tan^{-1}\left(\frac{Im\,\rho(t)}{Re\,\rho(t)}\right) \tag{5}$$

The phase and power signals will have a mean and a fluctuating component, $P = P_o + \tilde{P}$ and $\phi = \phi_o + \tilde{\phi}$. Generally $\phi_o = $ const. while P_o ranges between 0 and 1.

It is implicit in this model that the incident and reflected microwave beams are not affected by plasma fluctuations in front of the cutoff layer. Plasma refraction can bend and spread the beam profile, however refraction is not explicitly considered here since it is a machine dependent effect. However it's effects could be quantified with ray-tracing codes and then incorporated through adjustments to the beam radius and the angles of incidence and scattering.

3. ASYMMETRY

There are two forms of asymmetry that can affect reflectometer behaviour, (a) asymmetry in the reflectometer geometry (misalignment), i.e. different launch and receive angles, and (b) asymmetry (distortions) in the shape of the surface perturbations. Here the term distortion is used to

4

mean a deformation to a symmetric sinewave type perturbation, or to a Gaussian distributed random perturbation.

3.1 Misalignment

The launch and receive angles θ_1 and θ_2 can have any value between $\pm\pi$ in any combination. However the four basic combinations of angles shown schematically in figure 2 cover all experimentally encountered situations:
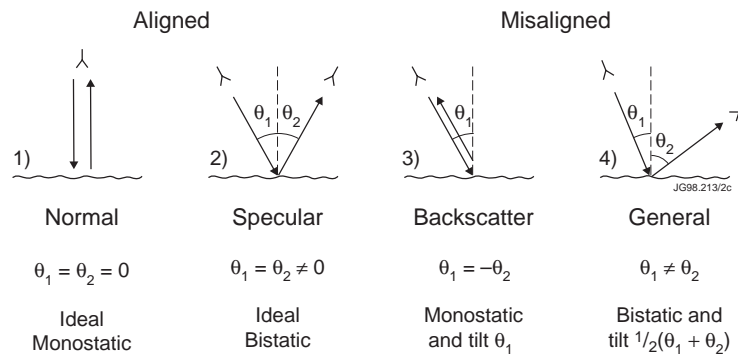

Figure 2 : Schematic showing four possible categories for the asymmetries in the reflectometer geometry; (a) Normal incidence and reflection, $\theta_1 = \theta_2 = 0$ (b) Specular reflection, $\theta_1 = \theta_2 \neq 0$ (c) Non-normal backscatter, $\theta_1 = -\theta_2 \neq 0$ (d) Asymmetric scattering, $\theta_1 \neq \theta_2 \neq 0$.

(1)   Normal incidence and reflection: $\theta_1 = \theta_2 = 0$. This is a monostatic configuration, i.e. a single antenna for both launch and receive beams. It is also the simplest, and perhaps the most widely studied idealized configuration. The received signal will contain both a specular (coherent) and a diffuse (incoherent) component.

(2)   Specular reflection: $\theta_1 = \theta_2 \neq 0$. This is the idealized configuration for a bistatic reflectometer, that is separate antennas for the launch and receive beams. Again the received signal will contain a specular and diffuse component.

(3)   Non-normal backscatter: $\theta_1 = -\theta_2 \neq 0$. This is also a monostatic configuration, but now only the diffuse incoherent backscattered power along the incident sight-line will be received. The specular component is generally lost - depending on the value of θ_1 and the width of the scattered power lobe. This configuration is equivalent to the ideal monostatic configuration with an antenna misalignment or a tilted plasma layer.

(4)   Asymmetric scattering: $\theta_1 \neq \theta_2 \neq 0$. This configuration includes all other possible combinations. As in the previous case generally only the diffuse incoherent component is received. This configuration is also equivalent to the idealized bistatic configuration with an antenna misalignment, or a tilted plasma layer, (the angle of tilt being $(\theta_1 + \theta_2)/2$).

3.2 Distortions

The second category of asymmetry applies to the shape of the reflection layer perturbations. Previously symmetric single frequency sinewave perturbations were used to model coherent MHD type plasma modes [27] and random perturbations with symmetric Gaussian amplitude distributions to model broadband plasma turbulence [10]. However as indicated earlier, rotating magnetic islands might generate reflection layers with sawtooth shaped perturbations [16,29,30]. This effect can be modelled as a skewed or distorted sinewave where the surface displacement ζ is generated by:

$$\zeta(x,t) = h\cos\left(\frac{2\pi x}{\Lambda} - \frac{\pi}{4}S\cos\left(\frac{2\pi x}{\Lambda} + \varphi\right) + \omega t + \varphi\right) \tag{6}$$

S is a skew factor between ± 1.0 which distorts the sinewave into a smooth sawtooth perturbation. Λ is the perturbation wavelength ($v = \omega\Lambda/2\pi$) and φ is the perturbation phase.

Alternatively the sinewave amplitude could be distorted towards a more cusp like shape:

$$\zeta(x,t) = h\left\{\frac{1}{2^{(c-1)}}\left[\cos\left(\frac{2\pi x}{\Lambda} + \omega t + \varphi\right) + 1\right]^C - 1\right\} \tag{7}$$

where C is a cusping factor greater than 0. These two types of asymmetric perturbations are quite distinct and produce different responses in the reflectometer. The first type of distortion is to the distribution of the slopes (or gradients) of the perturbation, i.e. a non-symmetric probability density function (pdf) for $\zeta' = d\zeta/dx$. The second type of distortion is to the amplitude distribution, i.e. a non-symmetric amplitude ζ pdf.

For broadband turbulence the surface displacement ζ can be generated from a Fourier summation of sinewaves:

$$\zeta(x,t) = \frac{\sigma}{\zeta_{sd}}\sum_{i=1}^{N} h(k_i)\cos(k_i x + \omega_i t + \varphi_i) \tag{8}$$

with a linear dispersion relation $v = \omega_i k_i$. φ is a random phase with a uniform distribution between $\pm\pi$, while h(k) is the weighting or (poloidal) k-spectral profile, which in this work is defined as a Gaussian with half-width k_w and mean k_m:

$$h(k) = exp\left(\frac{k - k_m}{k_w}\right)^2 \tag{9}$$

The summation is normalized by the standard deviation displacement ζ_{sd} to give a unity standard deviation, then scaled by the amplitude factor σ.

Again, the two types of distortions to the layer perturbations (asymmetric amplitude pdf and asymmetric gradient pdf) can be applied to the broadband fluctuations. Figure 3 illustrates

6

some example surfaces and probability density functions for six categories of possible perturbations. A surface with a preponderance of either negative or positive going spikes would result in an asymmetric amplitude distribution, while random sawteeth would result in an asymmetric gradient distribution. Both types of sequences are commonly observed in the ion-saturation currents from Langmuir probe diagnostics. For example, the surface can be made either spiky or sawtoothed by multiplying ζ with exponential functions such as

$$\zeta = \zeta \times (\exp(C\ \zeta) + 1) \tag{10}$$

$$\zeta = \zeta \times (\exp(S\ \zeta') + 1) \tag{11}$$

prior to normalization. C and S are the cusping and skewing factors with values between ±200.
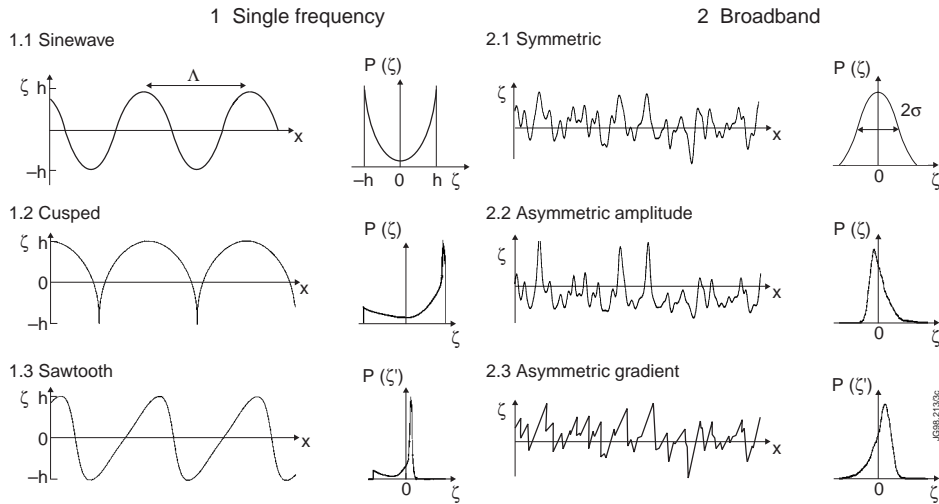

Figure 3 : Schematic showing six possible categories of surface perturbations. Left: (1) Single frequency mode, Right: (2) Broadband turbulence. Top row: symmetric perturbation, middle row: asymmetric amplitude distribution p(ζ) (cusped), bottom row: asymmetric gradient distribution p(ζ') (skewed).

4. RESULTS

Initially it appears that there are a multitude of different possible scenarios to be considered - four different antenna configurations combined with various types of surface perturbations, multiplied by two for single frequency modes and for broadband turbulence. Fortunately the simulations show that only two antenna geometries need be considered - aligned and misaligned. Normal incidence and specular reflection are both aligned geometries, $\theta_1 - \theta_2 = 0$. They give the same results irrespective of the surface perturbation when the amplitude is replaced with $h\cos\theta_1$. Backscatter is just a special case of the more general asymmetric scattering, both are misaligned with $\theta_1 - \theta_2 \neq 0$. The degree of misalignment $|\theta_1 - \theta_2|$, irrespective of whether it results from antenna misalignment or plasma layer tilt, is the salient parameter. Further, all possible forms of surface perturbations, single frequency and broadband, can be categorized by two parameters quantifying the degree of asymmetry in the distribution of their amplitudes and their gradients.

These three basic categories - misalignment, asymmetric amplitudes, asymmetric gradients - can be combined in a variety of ways to generate just about all possible experimentally conceivable scenarios. However as will be shown in the following case studies, where misalignment is combined with one or other form of distortion to single frequency and broadband fluctuations, these scenarios are generally just linear combinations of more basic features relating to each form of asymmetry.

The simulation model has six independent parameters: (i) The normalized perturbation amplitude, h/λ or σ/λ ($2h$ is the peak to peak mode amplitude, σ is the turbulent rms amplitude); (ii) The normalized perturbation wavelength Λ/λ or k_w/k_o in the case of turbulence; (iii) The normalized incident Gaussian beam radius w/λ; (iv) The transmit and receive angles θ_1 and θ_2; (v) C and (vi) S, the two factors which define the asymmetry in the perturbation amplitude and gradient distributions. Further, when the reflectometer has aligned geometry, $\theta_1 - \theta_2 = 0$, the wavelength and beam width parameters can be combined to form a single parameter Λ/w, or $k_w w$ in the case of turbulence with a Gaussian wavenumber spectrum.

4.1 Single frequency - Non-distorted sinewave - Aligned geometry

The case of normal incidence and reflection $\theta_1 = \theta_2 = 0$ has already been studied in some depth [27,31]. These results can be extended to the general aligned case by simply replacing the mode amplitude with $(h/\lambda) \cos\theta_1$, and adjusting the incident beam spot size to account for the elliptic footprint. (It should also be noted that large θ_1 and h/λ can lead to shadowing of the surface and hence the breakdown of the appropriate formulation for ζ.)

To briefly summarize, the reflectometer's phase and power response shows three distinct regions as a function of Λ/w.

(1) $\Lambda/w \gg 10$: For long wavelength fluctuations the surface appears flat. There is no attenuation and very little modulation in the reflected power ($P_o \rightarrow 1$, $\tilde{P} \rightarrow 0$) and the extent of the phase modulation $\delta\phi$ increases linearly with the mode amplitude as expected from geometric optics $\delta\phi = \pm 4\pi \cos\theta_1 h/\lambda$.

(2) $\Lambda/w < 1$: At very short fluctuation wavelengths the power is scattered into side-lobes resulting in strong attenuation of the reflected power and zero phase modulation ($\tilde{P} \rightarrow 0$, $\tilde{\phi} \rightarrow 0$).

(3) $1 < \Lambda/w < 10$: In the transition region, both P and $\delta\phi$ fall with decreasing Λ/w. The phase modulation no longer scales as predicted by geometric optics. The reflected power is modulated with a strong cusp-like shape at twice the frequency of the phase modulation, $f_P = 2f_\phi = 2f_{mode}$, i.e. no correlation between the phase and power fluctuations. See [24] for an experimental example.

8

4.2 Single frequency - Non-distorted sinewave - Misaligned geometry

The first major consequence of introducing asymmetry in the geometry is the loss of the specular zeroth order reflection with increasing θ_1. The rate of loss depends on the angular width of the zeroth order lobe, which scales inversely with the spot size w/λ [27]. The net effect is the progressive loss of reflected power at large Λ/λ (i.e. the reflectometer becomes insensitive to long fluctuation wavelengths) as shown in figure 4. Here the maximum P and ϕ are plotted as a function of Λ/λ with increasing backscatter angles (tilt) $\theta_1 = -\theta_2$ but fixed $h/\lambda = 0.1$ and $w/\lambda = 5$. Note the swelling in the phase response in the transition wavelength region.

As well as losing the long Λ/λ, the short wavelengths are also attenuated more severely than for specular reflection. However certain fluctuation wavelengths are not attenuated. These are the Bragg backscatter wavelengths given by

Figure 4 : Maximum reflected power P and phase ϕ vs normalized mode wavelength Λ/λ for various backscatter angles $\theta_1 = -\theta_2 = 0, 2.5, 5$ & 10° with fixed mode amplitude $h/\lambda = 0.1$ and spot size $w/\lambda = 5$.

$$\frac{\Lambda}{\lambda} = \frac{m}{(sin\theta_1 - sin\theta_2)} \quad (12)$$

where m is the diffraction order. For the aligned case, increasing the beam width w/λ simply translates the response curves to larger Λ/λ [31], but with misalignment increasing w/λ progressively causes the loss of both long and short fluctuation wavelength Λ sensitivity. Except at the Bragg wavelengths which become better defined with increasing w/λ with the Bragg backscattered power tending to a constant -6dB independent of the incident angle, and the phase response tending to a constant $\delta\phi = \pm m(\pi/2)$.

With misalignment both the phase and power time signals become distorted. Figure 5 shows P and ϕ as a function of the perturbation phase φ through one complete period with $w/\lambda = 2$, $\Lambda/\lambda = 5$, $\theta_1 = -\theta_2 = -2.5^o$ and increasing mode amplitude h/λ. As h/λ increases, the phase ϕ becomes more and more distorted around the zero crossing of the perturbation, $\varphi = 270^o$ (where the power is also seen to dip) until at some critical value h_c/λ the phase signal flips direction and begins to ramp continuously. This is the phase runaway effect so often observed in experiments [14-18,32,20] .
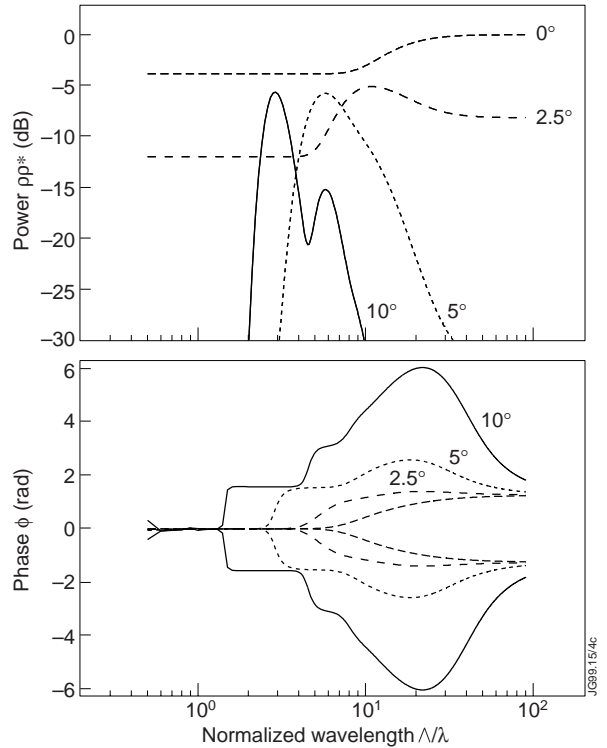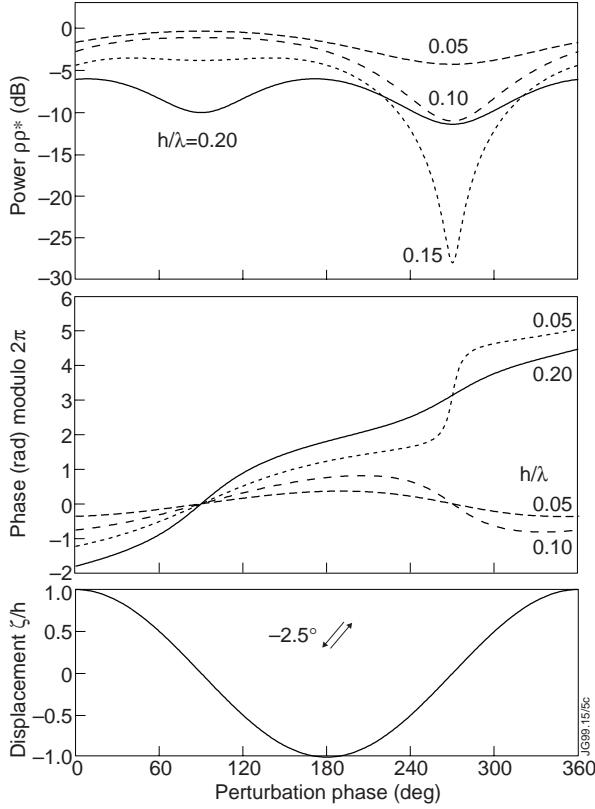
Figure 5 : Reflectometer power P and phase φ vs perturbation phase φ for increasing amplitude h/λ, with tilt θ₁ = −θ₂ = 2.5°, w/λ = 2 and Λ/λ = 5. Note phase runaway when h/λ > 0.14 Bottom trace shows normalized displacement ζ/h and arrows indicate incident and reflected beams.

The cause of the phase runaway, and the reason for the amplitude threshold h_c/λ becomes clear when the reflectometer signal is plotted in the complex plane. The time evolution of the complex reflection coefficient $\rho = A \exp(i\phi)$ ($A = \sqrt{P}$) will map out a trajectory in the complex/polar plane (Im ρ vs Re ρ or $A\sin\phi$ vs $A\cos\phi$). This "complex amplitude" plot has already been shown by some investigators to be an powerful analysis technique [13,32,19]. For a single frequency periodic perturbation the complex amplitude trajectory will follow a closed path through one complete perturbation period, starting and finishing at the same point. Figure 6 shows a series of complex amplitude plots for various conditions with $\Lambda/\lambda = 8$, $w/\lambda = 2$ and perturbation amplitudes between 0.05 and 0.25 (5% to 25%). Symmetric sinewave perturbations, figure 6(a), result in simple concentric arcs mirrored in the real axis (if $\phi_o = 0$). The crosses mark the beginning and the end of the perturbation period $\varphi = 0^o$. As h/λ
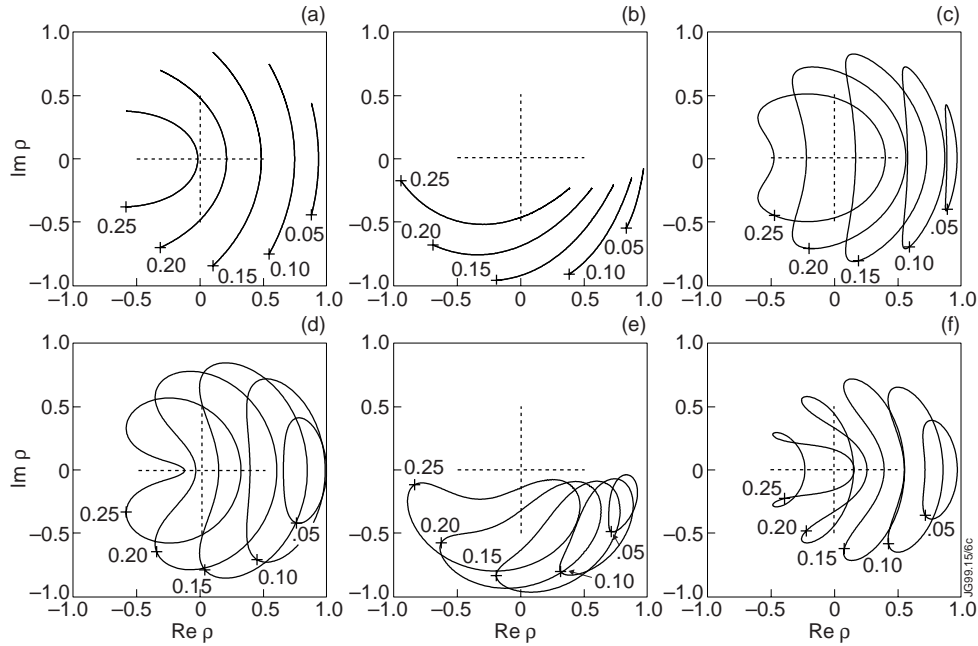

Figure 6 : Complex amplitude trajectory plots (Im ρ vs Re ρ) for single frequency perturbation with Λ/λ = 8, w/λ = 2 and increasing amplitude h/λ. Top row: no misalignment (a) Sinewave (b) Cusped C = 0.2, (c) Sawtooth S = −0.4, Bottom row: with tilt θ₁ = −θ₂ = 2.5° (d) Sinewave, (e) Cusped, (f) Skewed.

10

increases, the arc extends round to close on itself. This leads to phase wrapping at $\phi = \pm\pi$ but not to phase runaway since the trajectory must retrace its path (unwind in ϕ) back to the start point. Increasing the perturbation wavelength Λ/λ increases the radius $\rho\rho^* \approx 1$ but also moves the centre of curvature towards the origin.

When misalignment is introduced, figure 6(d), the trajectory does not retrace itself but opens out to form a closed loop. The size of the loop grows with increasing h/λ. If the loop encloses the origin then the phase ϕ can rotate through 2π in one perturbation cycle and phase runaway occurs.
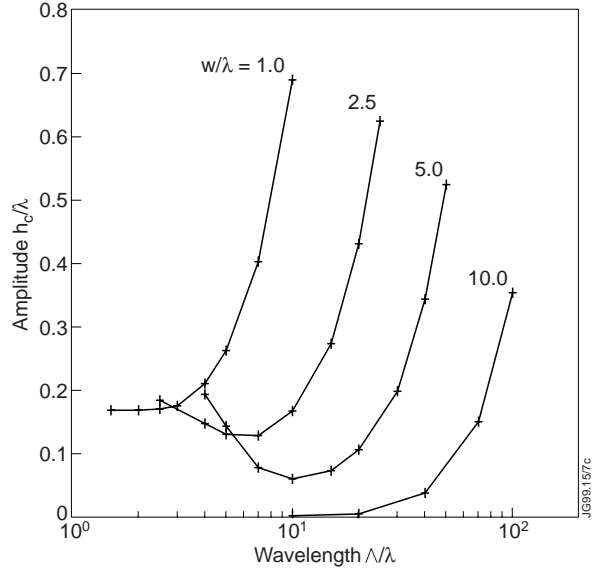

Figure 7 : Critical phase runaway fluctuation amplitude h_c/λ vs normalized wavelength Λ/λ for increasing beam width w/λ with fixed tilt $\theta_1 = -\theta_2 = 2.5^o$

The critical mode amplitude h_c/λ at which phase runaway starts varies with the perturbation wavelength, beam width, incident and scattering angles. Figure 7 shows h_c/λ as a function of Λ/λ for increasing beam width w/λ with $|\theta_1 - \theta_2| = 5^o$. (Since $\theta \approx \sin\theta$ for moderate angles the misalignment is expressed in terms of net angular difference $|\theta_1 - \theta_2|$). At long perturbation wavelengths or small beam widths $\Lambda > 10w$, the critical amplitude rises to infinity, i.e. there is no phase runaway in the 1D Geometric optics limit. At very short perturbation wavelengths $\Lambda \approx w$ the critical amplitude also rises, but here h_c/λ becomes difficult to discern because of the very small reflected power signal. The minimum in h_c/λ occurs at around $\Lambda \approx 2w$ and drops progressively in value with increasing w/λ. Increasing the misalignment $|\theta_1 - \theta_2|$ also reduces h_c/λ (almost to zero) and moves the minimum to larger Λ/λ.

In contrast to the aligned case where the power was always modulated at twice the frequency of the phase, figure 5 shows that below the critical amplitude the power P is modulated at the same frequency as the phase ϕ, i.e. correlated, but in quadrature (out of synchronization by $\pm\pi/2$). When the surface displacement ζ is maximum at $\varphi = 0^o$, P will be maximum at $\varphi = \pm90^o$ while ϕ is maximum at $\varphi = 180^o$. Above the critical amplitude the 2nd harmonic modulation reappears in both the power and phase signals.

For one complete perturbation period the reflectometer phase ϕ will always ramp by multiples of $\pm2\pi$ (depending on the dominant lobe order). The direction of ramping depends on the sign of angular difference $\theta_1 - \theta_2$ relative to the direction of the mode propagation.

4.3 Single frequency - Sawtooth distortion - Aligned geometry

The second class of asymmetries, that of distorting the sinusoidal perturbation, introduces several new effects. Figure 8 shows the reflected power P and phase ϕ (modulo 2π) through one period of a smooth sawtooth perturbation (skew factor S = 0.4) for normal incidence and

backscatter with increasing h/λ but fixed Λ/w = 5 : Again for the specular case the perturbation wavelength and beam radius can be combined.

For small amplitudes h/λ the phase φ replicates the shape of the perturbation, $\phi = -4\pi \cos\theta_1 \, \zeta/\lambda$. But as h/λ increases the phase becomes more and more distorted at the point of maximum surface gradient ($\varphi = 90^{\circ}$ in figure 8) and is accompanied by a sharp dip in the reflected power. When h/λ exceeds a critical value, φ reverses direction and begins to ramp in a similar manner to that due to misalignment. Figure 8 also shows that the power P is modulated at the same frequency as the phase φ (and hence correlated) but in quadrature ($\pm\pi/2$).

In the complex plane the signal trajectory again forms closed loops, figure 6(c), and again the point at which the trajectory encloses the origin marks the onset of phase runaway. The direction of the phase ramp depends on the relative direction of mode propagation and

Figure 8 : Reflectometer power P, phase φ (modulo 2π) and displacement ζ/h vs perturbation phase φ for sawtooth surface, S = 0.4 with normal incidence $\theta_1 = \theta_2 = 0$, Λ/w = 5 and increasing amplitude h/λ. Phase runaway occurs for h/λ > 0.17

the slope (or skew) of the sawtooth. The critical amplitude h_c/λ depends on the skew factor S as well as Λ/w. Figure 9 shows h_c/λ rising to infinity at large Λ/w for two values of skew S = 0.2 and 0.4. h_c/λ also tends to rise as Λ/w → 1. As in figure 7 for misalignment, phase runaway becomes more difficult to induce with small beam diameters.

The similarity between the sawtooth and the sinewave with misalignment is not unexpected. To a misaligned reflectometer the tilted surface of the sinewave will appear as a sawtooth profile when projected into the effective plane of the reflectometer beam. It is the net asymmetry in the apparent (or projected) surface gradient through one cycle of the moving perturbation that causes the complex amplitude trajectory to open into a loop, and hence lead to the possibility of phase runaway. However there is one major difference between the sawtooth and misalignment cases, there is no loss of reflected power (i.e. sensitivity) at long perturbation wavelengths with the sawtooth. This is illustrated in figure 10 which shows the maximum and minimum power and phase as a function of Λ/w with S = 0.4 and increasing h/λ. Also note the absence of Bragg backscatter enhancement with the sawtooth perturbation.
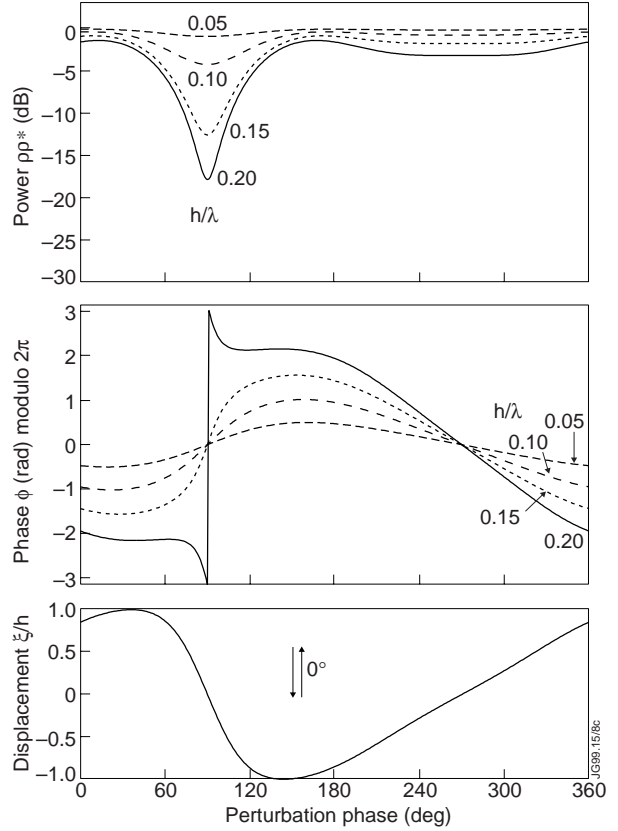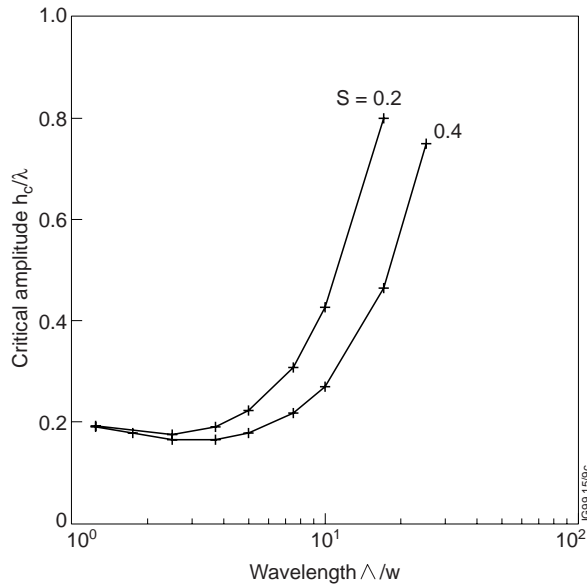
12

Figure 9 : Critical phase runaway fluctuation ampli-tude h_c/λ vs Λ/w at normal incidence $\theta_1 = \theta_2 = 0$, for sawtooth perturbation with S = 0.2 and 0.4
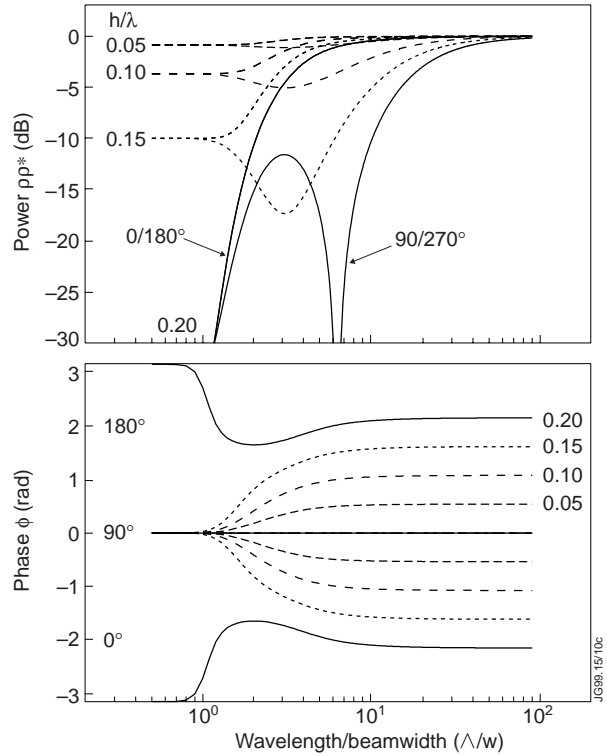

Figure 10 : Reflectometer power P and phase ϕ vs nor-malized wavelength Λ/w ($w/\lambda = 1$) at normal incidence for sawtooth S=0.4 at perturbation phases φ = 0, 90, 180, 270° and increasing amplitude h/λ.

4.4 Single frequency - Sawtooth distortion - Misaligned geometry

Individually, misalignment and sawtooth perturbations can both cause phase runaway if the perturbation amplitude is greater than some threshold. When combined, the result depends on the relative signs and magnitudes of S and $(\theta_1 - \theta_2)$. If S and $(\theta_1 - \theta_2)$ have the same sign (majority reflection off the shallow face of the sawtooth) then h_c/λ is substantially reduced for all wavelengths Λ/λ, and the power dip becomes deeper. For some values of $(\theta_1 - \theta_2)$, h_c/λ drops almost to zero. At small Λ/λ the phase ramp can be almost linear for all h/λ, while at large Λ/λ the phase can also ramp by multiples of 2π and display complex 2nd and 3rd harmonic modulations. Conversely if S and $(\theta_1 - \theta_2)$ are opposite in sign, then h_c/λ is raised and the reflected power is enhanced.

In all cases adding a misalignment to a sawtooth distortion again leads to a general loss of sensitivity at long perturbation wavelengths. The complex amplitude trajectory, figure 6(f), can form complicated loops and twists, but in all cases they remain symmetric about their mean phase, i.e. the real axis if $\phi_o = 0$.

4.5 Single frequency - Cusped distortion - Aligned geometry

The second form of surface distortion, the cusped or 'spiky' surface has a very different effect on the reflectometer signals. There is no phase ramping, but the phase response does depend on the shape of the cusps, particularly whether they are pointing outward (towards the antennas) or inward (away from the antennas) and on Λ/w.

13

Figure 11 shows the minimum and maximum P and ϕ as a function of Λ/w with $h/\lambda = 0.17$ and various cusping values from C=0.5 (inward cusps) to C=4 (outward cusps). C = 1 is the symmetric sinusoidal surface. At long perturbation wavelengths $\Lambda/w > 10$, the phase again follows the shape of the surface $\phi = -4\pi \cos\theta_1 \ \zeta/\lambda$, just as with the sinusoidal and skewed perturbations. However as Λ/w decreases two things happen. The phase modulation $\delta\phi \to 0$ as before, but the phase also acquires an offset $\phi_o \neq 0$. The phase offset ϕ_o changes sign as C increases from inward to outward cusps. The offset also varies non-linearly with h/λ as shown in figure 12 at $\Lambda/w = 1$. Secondly, P_o increases, i.e. there is less attenuation when there is cusping ($C \neq 1$).
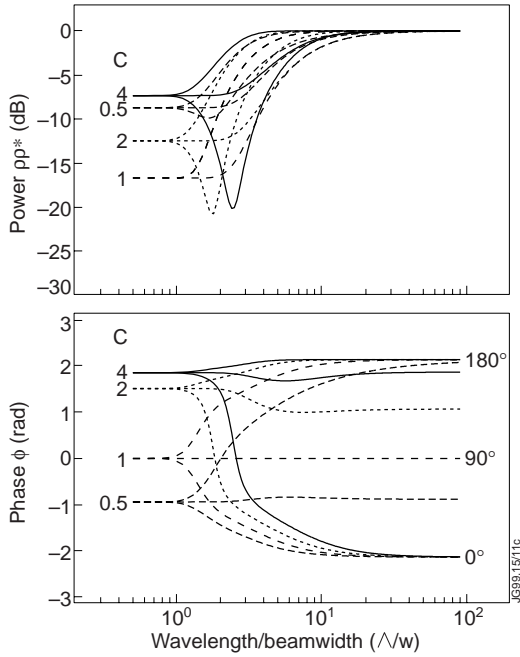

Figure 11 : Reflectometer power P and phase ϕ vs normalized wavelength Λ/w at normal incidence for C = 0.5 (inward cusped) through C = 1 (symmetric) to C = 4 (outward cusped) with fixed $h/\lambda = 0.17$ at perturbation phases $\varphi = 0, 90, 180^o$.
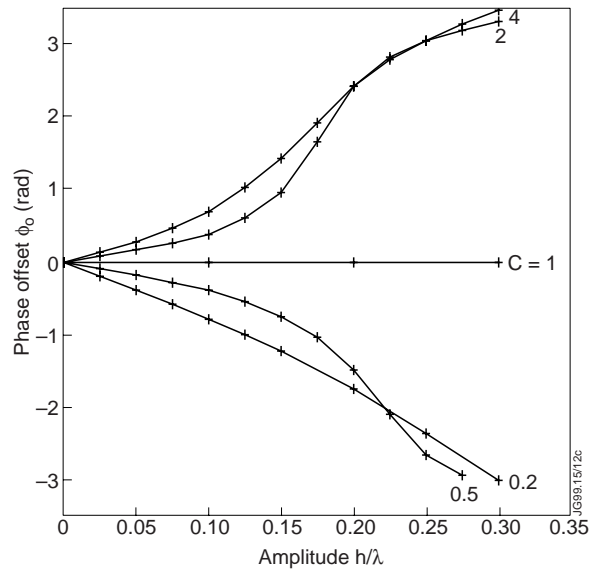
Figure 12 : Phase offset ϕ_o as a function of perturbation amplitude h/λ with $\Lambda/w = 1$ at normal incidence $\theta_1 = \theta_2 = 0$ for selected values of cusping.

Between $\Lambda/w \approx 2$ and 3 there is a pronounced increase in the modulation of the power signal. The degree of modulation and the perturbation wavelength Λ at which it occurs, increases with the value of C, i.e. the sharper the outward cusps or spikes. This is possibly due to some form of resonance between the beam diameter and certain perturbation wavelengths causing additional defocusing/focusing of the reflected beam, or perhaps because sharp outward spikes tend to make the surface appear more like a ruled grating.

The perturbation cusps, whether outward or inward, cause dips in the reflected power. Since these coincide with the cusps in the phase, $\widetilde{\phi}$ and $\widetilde{P}$ are thus correlated - with a relative cross-phase difference of 0 for outward cusps, and π for inward cusps.

In the complex amplitude trajectory of figure 6(b) for C=0.2 the phase offset and cross correlation are revealed as a non-linear rotation (and stretching) about the origin, clockwise for negative (inward) cusps, anti-clockwise for positive (outward) cusps. The offset arises from the inability of the microwave beam to penetrate all the way down into the depth of the inward cusp (same effect as waveguide cutoff), while for outward cusps the very narrow tops become invisible to the microwave beam. The effective surface displacement at the cusp approaches the mean value as the cusp becomes narrower.

4.6 Single frequency - Cusped distortion - Misaligned geometry

Adding an antenna misalignment to the cusp distortion results in some very strange behaviour in the phase and power signals. Figure 13 is an example of P and ϕ through one period of a negative cusp perturbation (C = 0.2) with a misalignment of $|\theta_1 - \theta_2| = 10^o$, long wavelength $\Lambda/\lambda = 20$, narrow beam $w/\lambda = 2$ and increasing perturbation amplitude. The phase offset is still evident, but also note how the phase and power maxima and minima move away from $\varphi = 180^o$ and become progressively more skewed and asymmetric with increasing h/λ.

Again as $|\theta_1 - \theta_2|$ increases there is the usual loss of reflectometer sensitivity at long and short perturbation wavelengths, and of course, above h_c/λ phase runaway occurs.

4.7 Broadband - Gaussian - Aligned geometry

The converse to the single frequency MHD mode is broadband random Gaussian turbulence. The case of normal incidence has also been previous studied in depth [10]. For completeness, and to provide a comparison for the asymmetry cases the results are briefly restated.

Figure 13 : Effect on reflectometer power and phase of adding surface tilt $\theta_1 = -\theta_2 = 5^o$ to cusped surface C = 0.2 with $\Lambda/\lambda = 20$ and $w/\lambda =2$. Bottom trace is displacement ζ/h as function of perturbation phase φ, arrows indicate beam directions.

(i) The phase fluctuations $\tilde{\phi}$ are symmetrically distributed (roughly Gaussian) about a zero mean $\phi_o = 0$, while the power fluctuations $\tilde{P}$ are non-symmetrically distributed. The level of reflected power P_o (i.e. carrier strength) varies inversely with the level (standard deviation) of phase fluctuations ϕ_{sd} and power fluctuations P_{sd}. See [24] for experimental example.
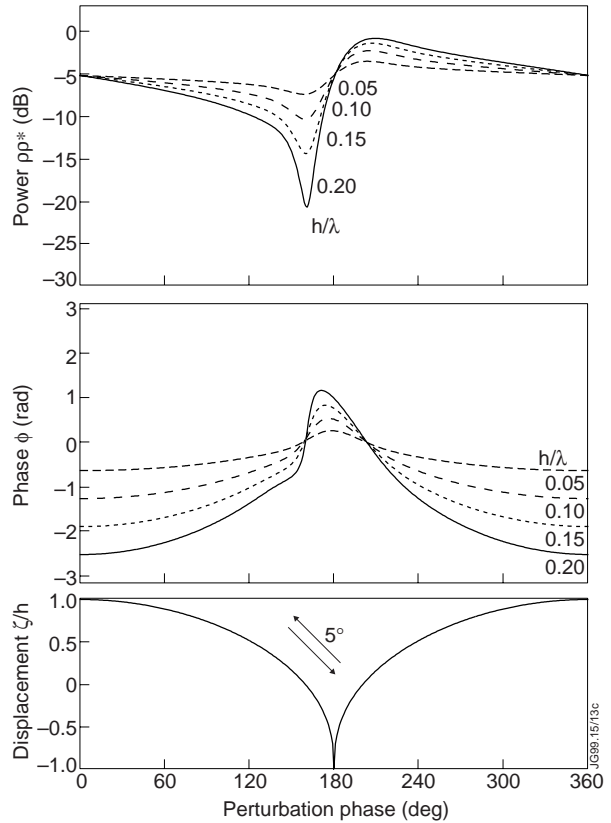
(ii)   For moderate fluctuation amplitudes $\sigma/\lambda \leq 0.1$ and large beam diameters $k_w . w > 2\pi$, the phase standard deviation (same as rms if $\phi_o = 0$) scales [24] with the rms amplitude of the turbulence σ/λ, the turbulence wavenumber spectral width k_w ($k_m = 0$), and the beam radius w as:

$$\phi_{sd} = \frac{4\pi\sigma}{\lambda} \frac{cos\,\theta_1}{\sqrt{2}} \left(\frac{k_w w}{2\pi} \right)^{-0.6} \qquad (13)$$

(iii) For $k_w . w \ll 2\pi$ the phase standard deviation scales as the 1D geometric optics limit $\phi_{sd} = 4\pi \cos\theta_1 \, \sigma/\lambda$; with $P_{sd} \to 0$ and $P_o \to 1$.

(iv)   For very large amplitude turbulence, i.e. $\sigma/\lambda > 0.2$, the phase fluctuations are uniformly distributed between $\pm\pi$ (which results in ϕ_{sd} saturating at 0.6π); P_o goes to 0 and $P_{sd}/P_o \to 1$. The fluctuation spectra of $\tilde{\phi}$ (and $\tilde{P}$ to a lesser extent) tend to a $1/f^2$ form.

The auto-correlation times ($C(\tau) = 1/e$) of both $\tilde{\phi}$ and $\tilde{P}$ scale directly with the beam width w and inversely (weakly) with k_w and (very weakly) with σ/λ. There is no correlation between the phase and power fluctuations for specular reflection.

4.8 Broadband - Gaussian - Misaligned geometry

As before, introducing any form of antenna misalignment moves the receiver off the specular axis of the scattered power lobe resulting in a decrease in the coherent reflection and an increase in the incoherent scattering. This is illustrated in figure 14 where (a) the phase standard deviation ϕ_{sd}, (b) mean power P_o and (c) relative power standard deviation P_{sd}/P_o are plotted as a function of the net misalignment angle $|\theta_1 - \theta_2|$ for increasing amplitude σ/λ with fixed $k_w/k_o = 0.5$ and $w/\lambda = 5$. Just a few degrees of misalignment are all that is necessary for the phase and power fluctuations to rise to saturation at $\phi_{sd} \to 0.6\pi$, and $P_{sd}/P_o \to 1$. Figure 14(b) illustrates how the specular return is lost with increasing σ/λ.
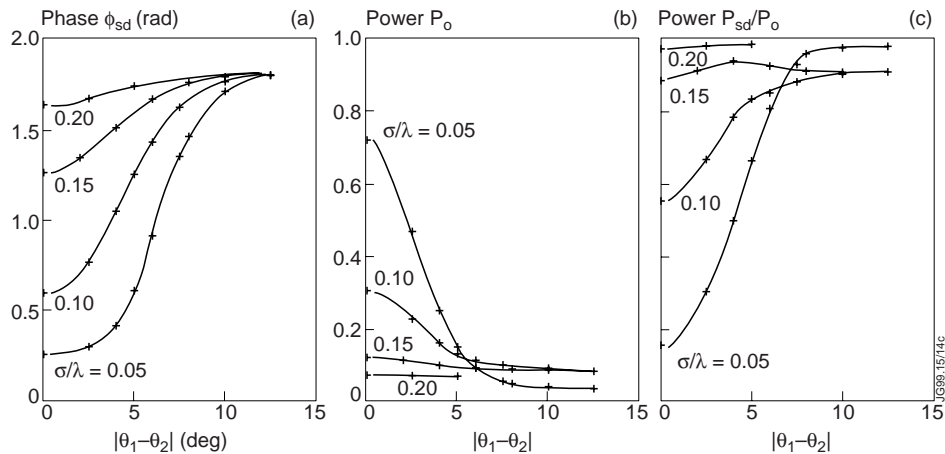

Figure 14 : (a) Phase ϕ_{sd}, (b) Mean power P_o and (c) Power P_{sd}/P_o as function of net misalignment angle $|\theta_1 - \theta_2|$ for increasing amplitude σ/λ with fixed $k_w/k_o = 0.5$ and $w/\lambda = 5$.

The rate at which ϕ_{sd} and P_{sd}/P_O saturate depends on the width of the scattered lobe. Figure 14 shows that the lobe broadens with increasing σ/λ, but increasing w/λ or k_w/k_o reduces the angular spread of the lobe.

In the single frequency perturbation, adding a surface tilt leads to phase runaway if the perturbation amplitude exceeds a certain value. The equivalent effect of phase runaway for a moving random perturbation is a Doppler shift ($f_D = d\phi/dt$) in the frequency spectrum of the phase fluctuations.
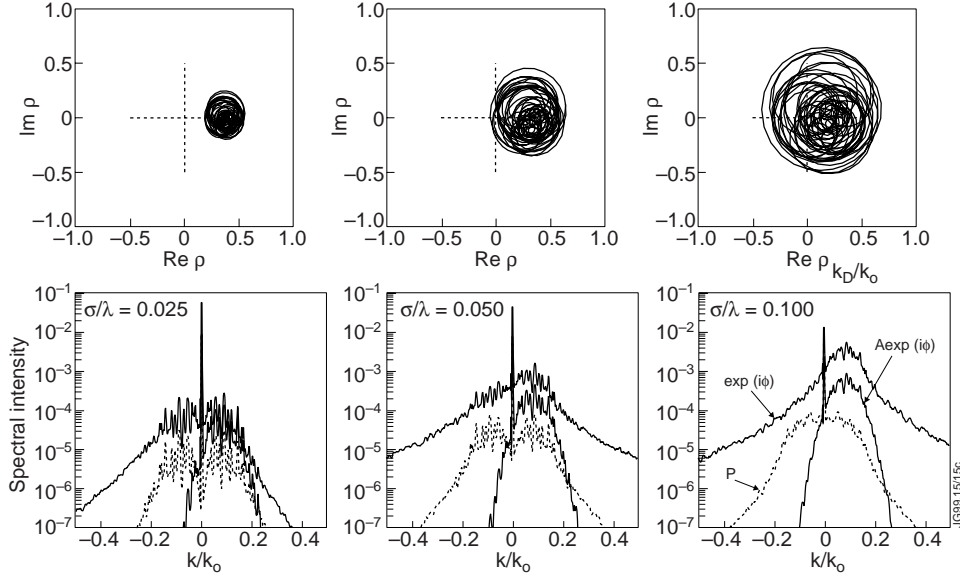

Figure 15 : Top row: Complex amplitude trajectory; Bottom row: Double-sided Fourier spectra for phase exp(iφ), power P, and complex amplitude Aexp(iφ) signals, for amplitude (a) σ/λ = 0.025, (b) 0.05 and (c) 0.10, with fixed k_w/k_o = 0.5, w/λ = 5 and $|θ_1 − θ_2|$ = 5°. Phase and complex amplitude spectra show Doppler shift at k_D/k_o.

Figure 15 shows the double-sided Fourier spectra (i.e. power spectra) of the phase ϕ, power P and complex amplitude $A\exp(i\phi)$ ($A = \sqrt{P}$) signals for three values of fluctuation amplitude σ/λ with k_w/k_o = 0.5, w/λ = 5 and $|\theta_1 - \theta_2|$ = 5°. The spectra are plotted in terms of normalized wavenumber $k/k_o = f/f_o \times c/v$ to remove the scaling of the transverse perturbation velocity v. Also plotted are segments of the complex amplitude trajectories. At large amplitudes σ/λ = 0.1, figure 15(c), the Fourier spectra of both the phase and complex amplitude signals show a clear Doppler shifted peak at

$$\frac{k_D}{k_o}\frac{v}{c} = \frac{f_D}{f_o} = \frac{v}{c}(sin\,\theta_1 - sin\,\theta_2\,) \tag{14}$$

The $\tilde{P}$ spectrum shows no Doppler shift and is symmetric about the peak at zero frequency (since P is a purely real signal). The complex amplitude trajectory circles around the origin which, as in the single frequency case, results in phase runaway.

As σ/λ decreases, figure 15(b), the complex amplitude trajectory moves away from the origin along the positive real axis. This is similar to figure 6(d) for the single frequency mode which shows that there is a σ_c/λ amplitude threshold for phase runaway. σ_c/λ behaves in a similar fashion as h_c/λ, it rises with decreasing w and k_w and falls with increasing misalignment $|\theta_1 - \theta_2|$.

Decreasing σ/λ below σ_c/λ leads to the appearance of a second peak at $-k_D/k_o$ in the $\tilde{\phi}$ spectrum and the formation of symmetric peaks at $\pm k_D/k_o$ in the $\tilde{P}$ spectrum. At σ/λ = 0.025, figure 15(a), the $\tilde{\phi}$ spectrum is almost symmetric resulting in a net zero frequency difference relative to the carrier frequency, i.e. the negative peak balances the positive Doppler peak, and hence no phase runaway.

The circular path of the complex amplitude trajectory results in the power (radius squared) being modulated at the same frequency as the phase - hence the strong peaks in the $\tilde{P}$ spectrum. Note however that the complex amplitude frequency spectrum still only displays one correct Doppler peak, whatever the turbulence amplitude.
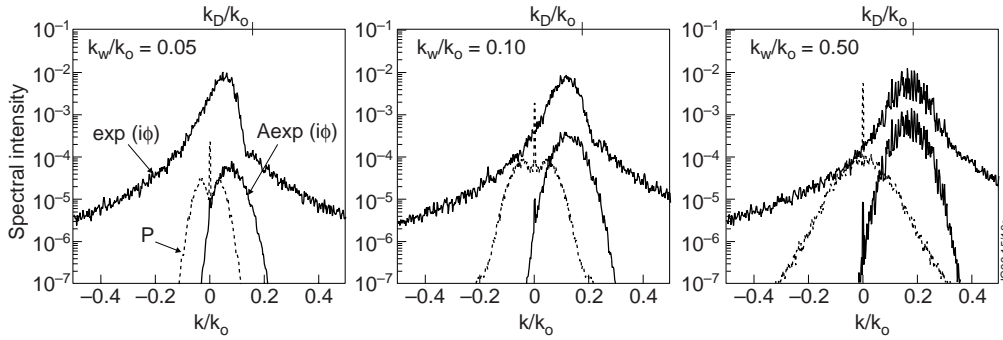

Figure 16 : Double-side Fourier spectra for phase exp(iφ), power P, and complex amplitude Aexp(iφ) signals for k_w/k_o = (a) 0.05, (b) 0.1 and (c) 0.5 with $|\theta_1 - \theta_2| = 10^o$, σ/λ = 0.1 and w/λ = 5.

Unfortunately this is not the whole story. The peak in the Aexp(iφ) spectrum may not necessarily be at the true Doppler frequency - even if phase runaway is evident and the $\tilde{\phi}$ spectrum has no negative (balancing) peak. Figure 16 shows three double-sided Fourier spectra for (a) k_w/k_o = 0.05, (b) 0.10 and (c) 0.50 with σ/λ = 0.1, w/λ = 5 and $|\theta_1 - \theta_2| = 10^o$. The Doppler peak should be at k_D/k_o = 0.174, but when the product of the spectral and beam widths $k_w . w < 2$, the high frequency part of the $\tilde{\phi}$ spectrum becomes truncated. The result is that the shift in the spectral peak does not reach the expected k_D in either the phase or complex amplitude spectra. At the same time the $\tilde{P}$ spectrum splits to form symmetric peaks at $\pm k_p$, the same position, as the $\tilde{\phi}$ spectral peak. This peak (relative to k_D) is plotted in figure 17 as a function of $k_w . w$ for various values of k_m/k_D where k_m is the mean wavenumber in the Gaussian distribution of equation 9. At large $k_w . w$ the spectral peak appears at the expected Doppler position, but as $k_w . w$ falls the peak moves towards the mean fluctuation wavenumber. This is to be expected since, as $k_w \rightarrow 0$ the surface perturbation approaches the single frequency case

(where $k_m = 2\pi/\Lambda$) which, with misalignment, showed both the power and phase to be modulated at the mode frequency. Likewise as $w \to 0$ the simulation approaches the 1D Geometric optics limit in which Doppler shifts do not appear.

Whenever there is a peak in the $\tilde{P}$ spectrum, such as at low fluctuation amplitudes $\sigma < \sigma_c$, or small wavenumber-beam widths $k_w .w < 2$ then there will also be a strong peak in the coherence γ^2 spectrum (between $\tilde{\phi}$ and $\tilde{P}$). For $\sigma < \sigma_c$, the coherence can approach unity. An example is shown in figure 18(a) where the Fourier, coherence, and cross-phase spectra are plotted for $\sigma/\lambda = 0.025$, $k_w/k_o = 0.5$, $w/\lambda = 5$

Figure 17 : Normalized spectral peak position k_p/k_D vs turbulence wavenumber width times beam width $k_w .w$ for various values of spectral mean k_m/k_D.

and $\left| \theta_1 - \theta_2 \right| = 5^o$. The dashed curve is the wavenumber spectrum h(k) of the surface perturbations.

Figure 17 gives the position of the principle γ^2 peak. In addition there are often smaller coherence peaks where there are no corresponding $\tilde{\phi}$ or $\tilde{P}$ spectral peaks. These peaks appear at Bragg backscatter wavenumbers:

$$\frac{k_B}{k_o} = \frac{f_B}{f_o}\frac{v}{c} = \frac{n}{m}(sin\theta_1 - sin\theta_2) \tag{15}$$

where n is the harmonic number, and m is the Bragg order. Note that the n/m = 2/2 Bragg peak coincides with the Doppler peak in $\tilde{\phi}$ spectrum. Figure 18(b) is an example which displays both Bragg peaks and a Doppler peak - in this case at $k_m/k_o = 0.2$ ($\sigma/\lambda = 0.1$, $k_w/k_o = 0.1$, $w/\lambda = 2$ and $\left| \theta_1 - \theta_2 \right| = 10^o$). Note how the relative cross-phase alternates between $+\pi/2$ and $-\pi/2$ with increasing harmonic number. The $\pm\pi/2$ phase difference appears as an anti-symmetric (about zero delay $\tau = 0$) time delayed cross correlation $C_{\phi P}(\tau)$.

As σ/λ increases the level of coherence around k_p is reduced. Significant coherence is only observed when the phase fluctuations are not saturated, $\phi_{sd} < 0.6\pi$, which generally means $\left| \theta_1 - \theta_2 \right| \leq 12^o$. For $\sigma > \sigma_c$ and $k_w .w$ above 2 there are no peaks in the $\tilde{P}$ spectrum, but as in the example of figure 18(c) substantial coherence at Bragg wavenumbers can still occur. [24] shows an experimental example.
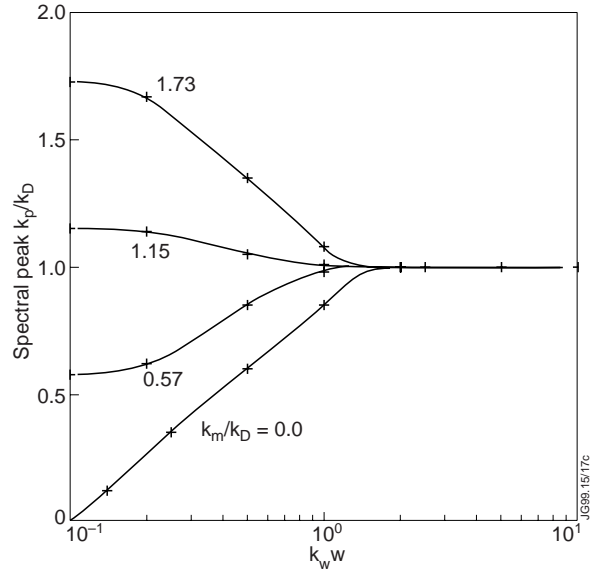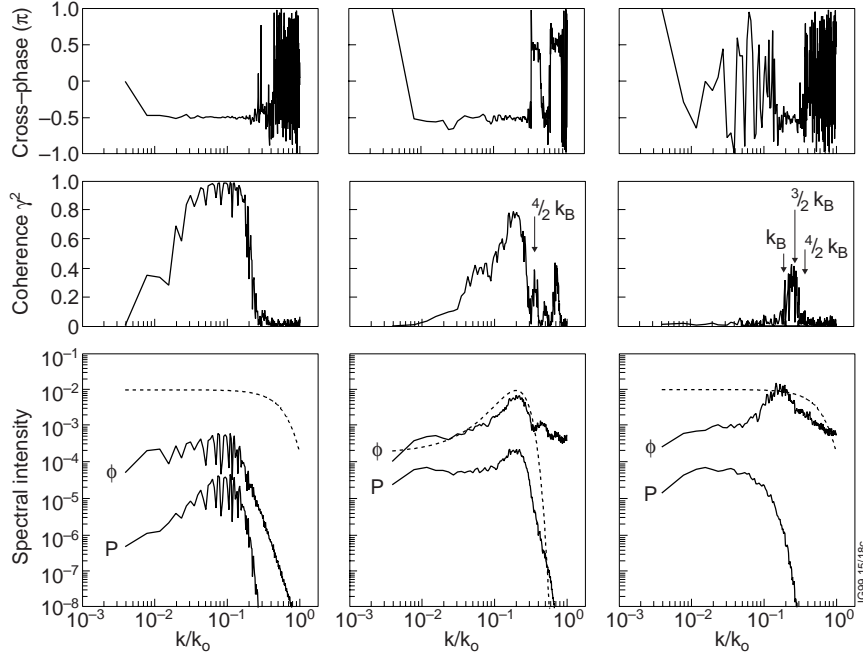
Figure 18 : Fourier spectra, γ^2 coherence and cross-phase spectra of broadband Gaussian perturbation with mis-alignment: (a) $\left|\theta_1 - \theta_2\right| = 5^o$, $\sigma/\lambda = 0.025$, $k_w/k_o = 0.5$, $w/\lambda = 5$; *(b)* $\left|\theta_1 - \theta_2\right| = 10^o$, $\sigma/\lambda = 0.10$, $k_w/k_o = 0.1$, $k_m/k_o = 0.2$, $w/\lambda = 2$; *and (c)* $\left|\theta_1 - \theta_2\right| = 10^o$, $\sigma/\lambda = 0.10$, $k_w/k_o = 0.5$, $w/\lambda = 5$. *The dashed line in the Fourier spectra is the surface perturbation k spectrum.*

4.9 Broadband - Cusped distortion - Aligned geometry

As for the single frequency mode, introducing cusping into the broadband perturbation, i.e. making the reflection layer spiky, leads to a phase offset $\phi_o \neq 0$ (non-zero mean) and a non-symmetric phase distribution (pdf). The direction (sign) and magnitude of the offset and skewness of the phase pdf depends on the degree of cusping and the amplitude σ/λ. Increasing σ/λ increases ϕ_o but decreases the skewness - note that the sign of the phase pdf skewness is opposite to that of the surface ζ pdf. In the complex amplitude trajectory the phase offset and skewness is seen as a rotation and a non-linear stretching of the trajectory in the polar direction, similar to that in figure 6(b) for the single frequency perturbation.

There are no peaks or shifts in any of the signal spectra, they remain symmetric about zero frequency; and, there is no phase runaway. However, as with the single frequency case where P and ϕ were both modulated in synchronous with the perturbation displacement ζ, the γ^2 coherence spectrum (between $\widetilde{\phi}$ and $\widetilde{P}$ fluctuations) shows substantial coherence for broadband cusped perturbations.

Figure 19(a) shows typical Fourier, γ^2 coherence, and cross-phase spectra for a cusped surface C = +20 with $\sigma/\lambda = 0.025$, $k_w/k_o = 0.2$ and $w/\lambda = 5$. The coherence spectra displays a series of γ^2 peaks at:

$$\frac{k_p}{k_o} = \frac{1}{2^n \pi k_w w} \tag{16}$$

20

for positive cusping C>1. If the cusping is negative, C<1, then equation 16 gives the positions of dips in γ^2 instead of peaks. This appears to be the same wavelength-beam width resonance phenomena observed in the single frequency cusped case. The peak positions are generally independent of the turbulence amplitude, but increasing σ/λ does decrease the level of coherence (maximum at around $\sigma/\lambda = 0.05$). The coherence also increases slightly with $k_w.w$ and the degree of cusping C.
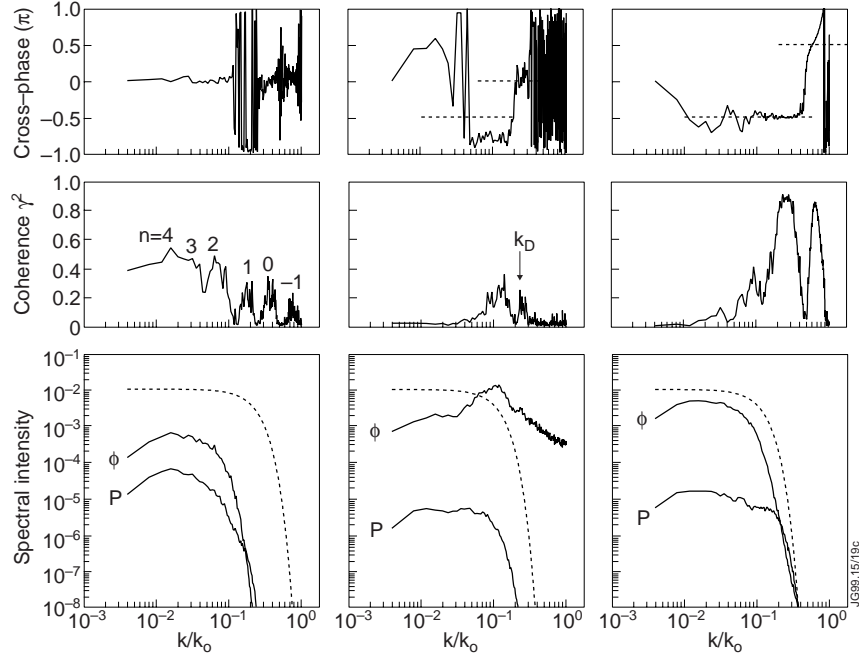

Figure 19 : Fourier spectra, γ^2 coherence and cross-phase spectra of (a) broadband cusped perturbation C = +20 with normal incidence $\theta_1 = \theta_2 = 0^o$, $\sigma/\lambda = 0.025$, $k_w/k_o = 0.2$ and $w/\lambda = 5$; (b) Cusped C = +20, $|\theta_1 - \theta_2| = 10^o$, $\sigma/\lambda = 0.05$, $k_w/k_o = 0.1$ and $w/\lambda = 5$; (c) Skewed S = +200, $|\theta_1 - \theta_2| = 0$, $\sigma/\lambda = 0.05$, $k_w/k_o = 0.1$ and $w/\lambda = 2$. Dashed line is the surface perturbation k spectrum.

The relative cross-phase difference is either 0 or π (and often alternates between successive γ^2 peaks). If the cusping is positive, i.e. upward spikes, then the cross correlation coefficient $C_{\phi P}(0)$ is positive and symmetric about $\tau = 0$ time delay; and the high n peaks have zero cross-phase difference. If the cusping is negative, i.e. downward spikes, then $C_{\phi P}(0)$ is negative and the high n peaks have $\pm\pi$ cross-phase difference.

4.10 Broadband - Cusped distortion - Misaligned geometry

Adding a small misalignment to the cusping leads to a combination of Doppler frequency shift and skewness in the phase distribution. The degree of the frequency shift is the same as for the misaligned non-distorted turbulence (with the same k_w/k_o cutoff and the same phase ϕ_{sd} broadening) while the phase skewness is the same as observed with the cusped-aligned case. Although the coherence is generally dominated by the misalignment, the cross correlation peaks become shifted in τ, i.e. the relative cross-phase difference is no longer exactly $\pm\pi/2$. The correlation is also non symmetric in magnitude as well as delay. Figure 19(b) shows a particularly

striking example for a misalignment of $|\theta_1 - \theta_2| = 10^o$ and C = +20. The first coherence peak is the (reduced) Doppler/Bragg peak due to the misalignment while the second γ^2 peak is due to the cusping. A possible experimental example is shown in [10].

4.11 Broadband - Sawtooth distortion - Aligned & misaligned geometry

Introducing asymmetry into the perturbation gradient distribution, for example making the reflection layer resemble random sawteeth, has basically the same effect as with the single frequency sawtooth perturbation. At low perturbation amplitudes there is again a strong correlation between $\tilde{\phi}$ and $\tilde{P}$ with a relative $\pm\pi/2$ phase difference. The coherence however does not appear at all wavenumbers but only in selected peaks, figure 19(c), which vary in position with k_w/k_o and w/λ. There are no peaks in either the $\tilde{\phi}$ or $\tilde{P}$ spectra at these positions. The $\tilde{\phi}$ spectrum is centred on zero frequency but there is an asymmetry or imbalance between the positive and negative high frequency tails - similar to the spectral truncation in figure 15(a) at low amplitudes with misalignment.

Increasing the amplitude σ/λ reduces the coherence, until at some critical value σ_c/λ (which as before decreases with increasing asymmetry factor S, beam width w/λ and k_w/k_o) the γ^2 peaks are destroyed and phase runaway begins.

Adding misalignment to the gradient asymmetry can again raise or lower the critical amplitude for phase runaway, and generate looped and indented bean shaped complex amplitude trajectories as in figure 6(f) for the single frequency mode.

5. DISCUSSION AND CONCLUSIONS

The simulations show that asymmetry can result in unexpected behaviour in the reflectometer response. This asymmetry can be in the geometry of the reflectometer launch and receive antennas, which is either:

(1)   Aligned : $\theta_1 - \theta_2 = 0$ (Specular reflection) or

(2)   Misaligned : $\theta_1 - \theta_2 \neq 0$ (Backscatter).

Or the asymmetry can be in the plasma reflection layer perturbations, which have either:

(3)   Symmetric amplitude and gradient probability density distributions,

(4)   Non-symmetric amplitude distributions (spiky or cusped),

(5)   Non-symmetric gradient distributions (sawtooth or skewed),

(6)   Non-symmetric amplitude and gradient distributions.

Each form of asymmetry has a distinct set of characteristic effects on the reflectometer response. For low to moderate fluctuation amplitudes, combining different asymmetries generally results in a simple addition of these basic features. However, at higher amplitudes, particularly above the critical value, complex interactions and modulations can appear in the signals. The basic features for the three types of asymmetry are summarized in Table 1. Some of these effects are straightforward, others require further comment.

Table 1 : Summary of effects introduced by the three categories of asymmetry on single frequency perturbation and broadband Gaussian perturbations.

Asymmetry	Single frequency	Broadband
Misalignment	Loss of coherent/specular return	Increase in ϕ_{sd} and P_{sd}
	Decrease in long Λ sensitivity	Doppler peaks in ϕ and $A\exp(i\phi)$ [a]
	Enhanced P at Bragg Λ	$\tilde{\phi}$ & $\tilde{P}$ coherent (γ^2) at Bragg k
	$f_P = f_\phi$ with $\pm\pi/2$ phase	with quadrature phase
	Phase runaway if $h > h_c$ [b]	Phase runaway if $\sigma > \sigma_c$ [b]
	2nd harmonic if $h < h_c$	High γ^2 if $\sigma < \sigma_c$
Asymmetric amplitude	Non-inear phase offset ϕ_o [c]	Non-symmetric $\tilde{\phi}$ pdf
	Increase in P at $\Lambda/w \leq 1$	$\tilde{\phi}$ skewness opposite ζ pdf
	Enhanced δP at $\Lambda/w \approx 2 - 3$	No spectral peaks but γ^2 coherence
	$f_P = f_\phi$ with 0 or π phase	with co- & counter phase [d,e]
Asymmetric gradient	Phase runaway if $h > h_c$	Phase runaway if $\sigma > \sigma_c$ [f]
	$\tilde{\phi}$ & $\tilde{P}$ correlate if $h < h_c$	γ^2 peaks with quadrature phase
	$f_P = f_\phi$ with $\pm\pi/2$ phase	if $\sigma < \sigma_c$ [d]

footnotes.

[a]   Doppler spectral shift depends on turbulence k_w and w/λ.

[b]   Critical amplitude depends on Λ/λ, $|\theta_1 - \theta_2|$ and w/λ (k_w/k_o).

[c] ϕ_o depends on sign and magnitude of amplitude asymmetry.

[d] γ^2 peaks vary with k_w and w, coherence decreases with increasing σ/λ.

[e]   Phase-power correlation is positive for upward cusps, negative for downward cusps.

[f]   Critical amplitude depends on degree of gradient asymmetry and Λ/w.

A Doppler shift with misalignment is expected, but the presence of a critical amplitude for phase runaway is less obvious. But when the signal trajectory is plotted in the complex plane the reason becomes apparent. Phase runaway can only occur if the fluctuation (sideband) amplitude exceeds the carrier wave amplitude. A similar phenomena appears in the FM capture effect in radio reception. Here, the stronger of two radio stations close in frequency will be demodulated while the weaker one will be suppressed [33]. There have been some recent attempts to use the Doppler shift in the $\tilde{\phi}$ spectrum to experimentally deduce the propagation velocity of the perturbations. However as figure 17 shows this can give misleading results if either the beam width or the spectral content of the perturbations is small. The shift in the $\tilde{\phi}$ spectral peak can only be considered a reliable measure of the Doppler frequency if there is no corresponding peak in the $\tilde{P}$ spectrum.

Doppler shifts and phase runaway are essentially 2D effects, and indeed the simulation results show that as the 1D limit is approached by reducing the beam radius $w \rightarrow 0$ then the

spectral peak in the phase goes to $f_m = v \times k_m/2\pi$ and the critical amplitude for phase runaway goes to infinity. In practical terms this means that phase runaway becomes less of a problem for small diameter (tightly focussed) reflectometer beams.

The enhanced modulation and phase-power coherence which appear at certain combinations of beam width and cusped/skewed perturbation wavenumbers is also an unexpected feature. It is clearly a 2D spatial resonance or interference effect, perhaps akin to Bragg backscatter.

The complex amplitude analysis shows that ignoring the amplitude fluctuations in the reflectometer signals - as has been an accepted practice for many years - is in fact worse than throwing away half the available information. Without knowledge of the power $\tilde{P}$, the phase $\tilde{\phi}$ signal can, potentially, be totally misinterpreted.

The simulations reveal a sufficient number of unique features in the signals to permit the experimentalist to identify the presence and types of asymmetries. These indicators include:

(1)   Phase runaway - which can only occur with large amplitude sawtooth perturbations or misaligned antennas.

(2)   Skewness in the distribution of phase fluctuations - which can only arise from cusped or spiky perturbations.

(3)   Correlation between the phase and power fluctuations.

Generally reflectometer signals display a degree of broadband background fluctuations with perhaps some well defined coherent MHD type oscillations. However peaks in the signal spectra do not, as the broadband simulations show, always correspond to coherent modes. But, when combined with the information in the coherence and cross-phase spectra, and other indicators such as the shape of the complex amplitude trajectory, it is possible to discriminate between the various asymmetry effects. Table 2 lists the possible combinations of peaks in the $A\exp(i\phi)$, ϕ, P, γ^2 and cross-phase spectra together with their interpretation.

When a misalignment or plasma tilt is combined with an asymmetric surface perturbation the simulation results suggest that it is possible to replicate almost any reflectometer fluctuation signal observed in experiments to date. In other words all experimentally observed features - phase ramping, $\tilde{\phi}$ and $\tilde{P}$ correlations, skewed $\tilde{\phi}$ distributions etc. could be explained and quantified in terms of reflectometer misalignment and asymmetric plasma cutoff layer perturbations.

Finally, it was previously shown that for symmetric perturbations and aligned geometry it is possible from measurements of the phase and power distributions together with knowledge of the beam width, to deduce the turbulence amplitude σ/λ and spectral content k_w/k_o, i.e. the transverse fluctuation correlation length [10]. Nevertheless even with the additional complications of antenna misalignment and perturbation asymmetry the latest results indicate that it may still possible to obtain σ/λ and k_w/k_o from the additional information in the higher order moments of the phase distribution, and the coherence and cross-phase spectra of $\tilde{\phi}$ and $\tilde{P}$.

Table 2 : Possible combinations of spectral peaks in the complex amplitude Aexp(iφ), phase φ, power P, coherence γ^2 and cross-phase C-P spectra together with their interpretation.

$Ae^{i\phi}$	ϕ	P	γ^2	C-P	Interpretation
P	P	-	-	-	True coherent mode, $\Lambda > 10w$, no misalignment
P	P	2nd	-	-	True coherent mode, $2w < \Lambda < 10w$, no misalignment
P	P	(2nd)	P+	0 or π	Coherent mode, cusped, no misalignment
P	P	(2nd)	P+	$\pm\pi/2$	Coherent mode, skewed, no misalignment
S/P	H/P	P	P	$\pm\pi/2$	Coherent mode, misaligned
-	-	-	P	0 orπ	Broadband, cusped
-	A	-	P	$\pm\pi/2$	Broadband, skewed
S	S	-	-	-	Broadband, misaligned, true Doppler
S	S	-	+	$\pm\pi/2$	Broadband, misaligned, true Doppler, Bragg
S	S/A	P	P	$\pm\pi/2$	Broadband, misaligned, reduced Doppler

P = Peak (coincident)
+ = Plus other non-coincident peaks
S = Shifted peak in double-sided spectrum, but will appear as (coincident) peak in single-sided spectrum
A = Asymmetric or truncated (double-sided spectrum)
2nd = 2nd harmonic
H = Many harmonics
() = May or may not be present depending on mode amplitude

ACKNOWLEDGEMENTS

REFERENCES

[1]   Proc. IAEA Workshop on Reflectometry for Fusion Plasmas (JET) 1992 (Abingdon: JET).

[2]   Proc. II IAEA Workshop on Reflectometry for Fusion Plasmas (Princeton) 1994 (New Jersey: PPPL).

[3]   Proc. III Workshop on Reflectometry for Fusion Plasmas (Madrid) 1997 (Madrid: CIEMAT)

[4]   Irby J H, Horne S, Hutchinson I and Stek P 1993 Plasma Phys. Control. Fusion **35** 601

[5]   Bruskin L G, Mase A and Tamano T 1995 Plasma Phys. Control. Fusion **37** 255

[6]   Vershkov V A, Dreval V V, Soldatov S V, Tsaun S V and Kartsev Y A 1995 22nd Eur. Conf. Control. Fusion Plasma Phys. (Bournemouth) vol 19C pt IV of ECA (Geneva: European Phys. Soc.) p401

[7]   Zhuravlev V, Sanchez J and de la Luna E 1996 Plasma Phys. Control. Fusion **38** 2231

[8]   Branas B, Hirsch M, Baldzuhn, Estrada T, Geist T, Hartfuss H J, Sanchez J and Zhuralev V 1996 23rd Eur. Conf. Control. Fusion Plasma Phys. (Kiev) vol 20A pt I of ECA (Geneva: European Phys. Soc.) p369

[9]   Irby J H and Stek P 1990 Rev. Sci. Instrum. **61** 3052

[10]   Conway G D, Schott L and Hirose A 1996 Rev. Sci. Instrum. **67** 3861

[11]   Conway G D 1997 Plasma Phys. Control. Fusion **39** 407

[12]   Cohen B I, Kaiser T B and Garrison J L 1997 Rev. Sci. Instrum. **68** 1238

[13]   Grossmann M T, Holzhauer E, Hirsch M, Serra F, Manso M E and Nunes I 1997 24th Eur. Conf. Control. Fusion Plasma Phys. (Berchtesgarden) vol 21A pt IV of ECA (Geneva: European Phys. Soc.) p1497. Holzhauer E et al 1998 Plasma Phys. Control. Fusion **40** 1869

[14]   Branas B, Hirsch M, Zhuravlev V, Sanchez J, de la Luna E, Estrada T, Geist T and Hartfuss H J 1995 22nd Eur. Conf. Control. Fusion Plasma Phys. (Bournemouth) vol 19C pt IV of ECA (Geneva: European Phys. Soc.) p161

[15]   Sips A C C and Kramer G J 1993 Plasma Phys. Control. Fusion **35** 743

[16]   Aleksandrov V O, Bulanin V V, Korneev D O and Sergeyev A A 1992 19th Eur. Conf. Control. Fusion Plasma Phys. (Insbruck) vol 16C pt I of ECA (Geneva: European Phys. Soc.) p111

[17]   Bulanin V V and Korneev D O 1994 Plasma Phys. Rep. **20** 14

[18]   Hanson G R, Harris J H, Wilgen J B et al 1992 Nucl. Fusion **32** 1593

[19]   Ejiri A, Shinohara K and Kawahat K 1997 Plasma Phys. Control. Fusion **39** 1963

[20]   Mazzucato E, Batha S F, Beer M, et al 1996 Phys. Rev. Lett. **77** 3145

[21]   Rhodes T L, Baang S, Chou A E, Luhmann Jr. N C and Peebles W A 1992 Rev. Sci. Instrum. **63** 4599

[22]   Estrada T, Sanchez J, Hartfuss H J, Hirsch M and Geist T 1993 20th Eur. Conf. Control. Fusion Plasma Phys. (Lisboa) vol 17C pt I of ECA (Geneva: European Phys. Soc.) p369

[23]   Hirsch M et al 1997 Proc. III Workshop on Reflectometry for Fusion Plasmas (Madrid) 1997 Informes Tecnicos Ciemat **838** p21 (Madrid: CIEMAT)

[24]   Conway G D 1997 Proc. III Workshop on Reflectometry for Fusion Plasmas (Madrid) 1997 Informes Tecnicos Ciemat **838** p39 (Madrid: CIEMAT). Also [JET report JET-P(97)14]

[25]   Conway G D, Vayakis G and Bartlett D 1997 Proc. III Workshop on Reflectometry for Fusion Plasmas (Madrid) 1997 Informes Tecnicos Ciemat **838** p1 (Madrid: CIEMAT). Also JET report JET-P(97)13

[26]   Sanchez J, Branas B, de la Luna E and Estrada T 1993 Rev. Sci. Instrum. **64** 487

[27]   Conway G D 1993 Rev. Sci. Instrum. **64** 2782

[28]   Beckmann P and Spizzichino A 1963 The Scattering of Electromagnetic Waves from Rough Surfaces (Oxford: Pergamon)

[29]   Bulanin V V, Korneev D O and Dreval V V 1993 20th Eur. Conf. Control. Fusion Plasma Phys. (Lisboa) vol 17C pt IV of ECA (Geneva: European Phys. Soc.) p1517

[30] Clairet F, Moreau P, Paume M and Chareau J M 1997 24th Eur. Conf. Control. Fusion
       Plasma Phys. (Berchtesgarden) vol 21A pt I of ECA (Geneva: European Phys. Soc.) p237

[31] Conway G D 1997 Plasma Phys. Control. Fusion **39** 1261

[32] Shinohara K, Shiraiwa S, Hishino K, Miura Y, Hanada K, Toyama H and JFT-2M Group
       1997 Jpn. J. Appl. Phys. **36** 7367

[33] Collings S 1997   Simon Collings, Radio Communications Consultant, Web page: http://
       wkweb4.cableinet.co.uk/simon.collings/Modulation/FM.htm